# Skyrmion lattice hosted in synthetic antiferromagnets and helix modes

X.-G. Wang,[1] L. Chotorlishvili,[2,3] G. Tatara,[4,5] A. Dyrdał,[6] Guang-hua Guo,[1] V. K. Dugaev,[2] J. Barnaś,[6,7] S.S.P. Parkin,[8] and A. Ernst[8,9,10]

[1]*School of Physics and Electronics, Central South University, Changsha 410083, China*
[2]*Department of Physics and Medical Engineering, Rzeszów University of Technology, 35-959 Rzeszów, Poland*
[3]*Faculty of Mathematics and Natural Sciences, Tbilisi State University, Chavchavadze av. 3, 0128 Tbilisi*
[4]*RIKEN Center for Emergent Matter Science, 2-1 Hirosawa, Wako, Saitama 351-0198, Japan*
[5]*RIKEN Cluster for Pioneering Research, 2-1 Hirosawa, Wako, Saitama 351-0198, Japan*
[6]*Faculty of Physics, Adam Mickiewicz University, ul. Uniwersytetu Poznańskiego 2, 61-614 Poznań, Poland*
[7]*Institute of Molecular Physics, Polish Academy of Sciences, ul. M. Smoluchowskiego 17, 60-179 Poznań, Poland*
[8]*Max Planck Institute of Microstructure Physics, Weinberg 2, D-06120 Halle, Germany*
[9]*Institute for Theoretical Physics, Johannes Kepler University, Altenberger Straße 69, 4040 Linz, Austria*
[10]*Donostia International Physics Center (DIPC), 20018 Donostia-San Sebastián, Basque Country, Spain*

(Received 28 November 2021; revised 1 September 2022; accepted 1 September 2022; published 20 September 2022)

Thin ferromagnetic films can possess unconventional magnetic properties, opening a new road for using them in spintronic technologies. In the present work exploiting three different methods, we comprehensively analyze phason excitations of a skyrmion lattice in synthetic antiferromagnets. To analyze phason excitations of the skyrmion lattice, we have constructed an analytical model based on three coupled helices and found a linear gapless mode. Micromagnetic simulations also support this result. Moreover, a similar result has been achieved within the rigid skyrmion lattice model based on the coupled Thiele's equations, when the coupling between skyrmions in different layers of the synthetic antiferromagnetic is comparable to or larger than the intralayer coupling. In addition, we also consider the orbital angular momentum and spin pumping current associated with phason excitations. Due to the gapless excitations in the case of skyrmion lattice, the pumping current is nonzero for the arbitrary frequency of pumping microwaves. In the case of individual skyrmions, no current is pumped when microwave frequency is inside the gap of the spectrum of individual skyrmions.

DOI: 10.1103/PhysRevB.106.104424

## I. INTRODUCTION

There is currently a great interest in two-dimensional topological solitons (skyrmions) and in ordered skyrmion lattices, known also as skyrmion crystals (SkX) [1–15]. It is well established that the dominant interaction leading to skyrmion formation is the Dzyaloshinskii-Moriya (DM) coupling that occurs in magnets with no spacial inversion symmetry. This coupling lowers the ground-state energy of the system and thus stabilizes the skyrmion magnetic textures. Formation of SkXs in thin films is energetically more favorable than formation of individual skyrmions. A key problem is a search for materials hosting SkXs. In what follows, we will explore the formation of SkXs and also their dynamical properties in a synthetic antiferromagnet (SAF), i.e., in a system consisting of two ferromagnetic layers coupled antiferromagnetically. Individual skyrmions in such materials were investigated very recently [16].

Before proceeding to the main objectives of this paper, we briefly recall the key features of the magnonic spectrum of ferromagnets with individual skyrmions and with SkXs. The dynamical properties of individual skyrmions are studied in Refs. [17–19]. It was shown that the spectrum of low-energy excitations in a ferromagnetic layer hosting a single static skyrmion includes a magnon mode with an energy gap [17]. The dispersion of this mode is $\omega(p) = \omega_0(a/R)^2 + \omega_0 a^2 p^2$, where $\omega_0$ is the stiffness frequency related to the exchange interaction, $R$ is the skyrmion radius, $a$ the lattice parameter, and $p$ is the radial momentum. Inside the frequency gap, $\omega_0(a/R)^2$, there appear two localized states, related to the bound skyrmion-magnon breathing and quadrupole modes [17]. Since the energy of a system with a single skyrmion does not depend on the position of the skyrmion, there is also a zero energy mode associated with the skyrmion drift: a skyrmion can move as a massless particle in a gauge field.

In the case of an SkX, the continuous symmetry of the system is broken. Nevertheless, in-plane translations of the SkX lattice as a whole do not change the system's energy, which leads to a gapless magnon mode corresponding to the deformation waves in the SkX lattice. Naturally, these magnon modes can be associated with the gapless Nambu-Goldstone excitations [20], which appear at the phase transition breaking the initial symmetry of Lagrangian. This problem has been discussed in a number of publications [21–34].

A central problem in the magnonic spintronics is the rectification and control of the magnonic spin current [35–37]. Direction of this current can be switched by an external magnetic field [37]. However, the magnetic field increases the gap in the magnon spectrum and thus reduces the number of magnons contributing to the magnonic spin current. In the present work, we show that the gapless spectrum of SkX allows switching of the spin current without reducing its

 

magnitude. Apart from this, due to swirling of the magnetization texture in the SkX, the net spin current in both layers of a SAF is nonzero, while it vanishes in the SAF without SkX. Thus, SkX in a SAF may serve as a unique platform for manipulating spin currents in spintronic devices.

Generally, the free energy of a ferromagnetic system, as a function of the unit vector $\mathbf{m}$ pointing along the magnetization, can be written in the form [21]

$$F_{SkX}[\mathbf{m}(\mathbf{r})] = \int [A_{\rm ex}(\nabla \mathbf{m}(\mathbf{r}))^2 - \mu_0 M_s m_z H_z + a_m \mathbf{m}^2(\mathbf{r}) + b_m \mathbf{m}^4(\mathbf{r}) + E_{DM}] d^2\mathbf{r}, \quad (1)$$

where the first and second terms correspond to the exchange and Zeeman energy, respectively, where $M_s$ is the saturation magnetization and $A_{\rm ex}$ is the exchange stiffness parameter. The last term, $E_{DM} = D[(m_z \frac{dm_x}{dx} - m_x \frac{dm_z}{dx}) + (m_z \frac{dm_y}{dy} - m_y \frac{dm_z}{dy})]$, stands for the interfacial DM energy and breaks symmetry in the $\mathbf{z}$ direction. The free energy of an SkX also includes the Ginzburg-Landau terms, $a_m \mathbf{m}^2(\mathbf{r})$ and $b_m \mathbf{m}^4(\mathbf{r})$, that generally are essential for stabilization of the magnetization. The Ginzburg-Landau energy, Eq. (1), is valid close to the Curie temperature, $T_c$, and was used to argue stabilization of the skyrmion lattice structure by a quartic term $\sim m^4$ [21]. Thus this approach accounts for the emergence of SkX near $T_c$. Until recently, SkX has been shown to appear in various temperature regimes due to different stabilization mechanisms. In this paper, however, we will not deal with the stabilization mechanisms of the SkX, so we assume that the three-helix state [see Eq. (3) in the following section] is a good approximation.

It has been shown that a SkX can be considered as a superposition of three coupled helices [38–40]. At temperatures below a critical temperature of transition to the trivial magnetic phase and for intermediate magnetic fields, the description based on three magnetic helices is well justified [40]. A ferromagnetic layer with a single helix and with coupled helices was studied in [25]. It was shown there that the quadratic part of the free energy for a single helix can be diagonalized exactly, and below the critical value of $a_m$, $a_m < D^2/(4A_{ex})$, the ground state is a single helix with the energy $\epsilon(k) = a_m + A_{ex}k^2 - Dk$, which is minimized for $k = D/2A_{ex} \equiv Q$. Small excitations from the ground state have been considered in terms of the Euler-Lagrange equations for the Lagrangian function $L = L_B - U$, where $L_B$ stands for the relevant Berry phase term, which plays the role of kinetic energy, while $U$ takes into account energy due to magnetization deviations from the ground state. A simple analytical formula was found for spin-wave propagation along the helix, with the corresponding dispersion relation $\omega(p) = (2A_{ex}\gamma M_s)\sqrt{Q^2p^2 + p^4}$, where $\gamma$ is the gyromagnetic ratio. The spectrum is gapless and linear in the low-energy limit, i.e., for $p \ll Q$. To study coupled helices, an external magnetic field was assumed, that induces a finite uniform magnetization. Owing to this, the quartic term in the free energy could be rewritten as an effective cubic term, which couples the three helices [25]. Two types of modes were discovered: (i) longitudinal waves, $\omega_l = A_{ex}\gamma M_s\sqrt{3Q^2p_{in}^2 + 2p_{out}^4}$, associated with the displacement of the SkX parallel to the in-plane component of the wave vector $\mathbf{p}_{in} = (p_x, p_y, 0)$, and (ii) transverse waves, $\omega_t = A_{ex}\gamma M_s\sqrt{Q^2p_{in}^2 + 2p_{out}^4}$, with the displacement along $\hat{\mathbf{z}} \times \mathbf{p}_{in} = (-p_y, p_x, 0)$, where $\hat{\mathbf{z}}$ is a unit vector along the axis $z$, and $p_{out}$ is the out-of-plane ($z$) component of the wave vector. For details see Ref. [25].

In the present work we explore the phason excitation spectrum in the SAF (see Fig. 1). Phasons are excitations corresponding to a phase degree of freedom of the collective structures, proposed originally in [41]. In-plane translations of the SkX lattice conserve the system's energy, while continuous symmetry within the SkX is broken. The gapless sliding phason modes in the SkX lattice are equivalent to the gapless Nambu-Goldstone excitations mentioned above. The idea is general for any structure with periodicity. In fact, for a periodic structure $\sim \sin(kx)$ along the $x$ direction and with a wavelength $k$, shifting the coordinate center by a time-dependent position $X(t)$ leads to a dynamic phase $\varphi(t) \equiv kX(t)$, as $\sin[k(x - X(t)] = \sin[kx - \varphi(t)]$. The phason excitations can also be described by a standard perturbative expansion of fluctuations [25]. However, the approach used in [22] for description of the phason modes is useful for physical interpretation of the structure dynamics, and also for comparison of analytical results and experimental observations. We note that the nontrivial magnetic texture of antiferromagnetic skyrmions promotes a nonvanishing topological spin Hall effect [42]. The SAF is composed of nanometer-thick ferromagnetic layers, which are coupled antiferromagnetically through a nonmagnetic spacer layer. The coupling mechanism arises from the Ruderman-Kittel-Kasuya-Yosida (RKKY) interaction. The heavy-metal-ferromagnet interfaces lead to the DM interaction in the SAF. Skyrmions in SAFs are stabilized by the DM interaction and bias magnetic fields from other neighboring layers. We analyze the magnetic dynamics using different approaches.

The work is organized as follows: In Sec. II we generalize the method based on coupled helices to study phason excitation in the SAF case. In Sec. III we present results of micromagnetic simulations. The obtained results are consistent with those based on the coupled helices model. In turn, in Sec. IV we present a Thiele's equation approach for a single ferromagnetic layer and for two layers coupled antiferromagnetically (SAF system). We also discuss the differences between the methods. The Thiele's equations treat skyrmions as rigid objects, thereby neglecting magnetization dynamics inside the skyrmion magnetic texture. The SkX in a SAF is modeled in this approach as a lattice of interacting individual skyrmions. In comparison, the coupled helices model is relevant for the strongly interacting and correlated phase, where the concept of individual skyrmions is irrelevant. Despite this, we show that the approach based on Thiele's equation leads to results which are consistent with those obtained by other techniques. A summary and final conclusions are presented in Sec. V.

## II. SPECTRUM OF PHASON EXCITATIONS IN A SAF

It is known that ferromagnetic or antiferromagnetic ordering is not possible in one- or two-dimensional Heisenberg systems with finite-range interaction [43] (see also

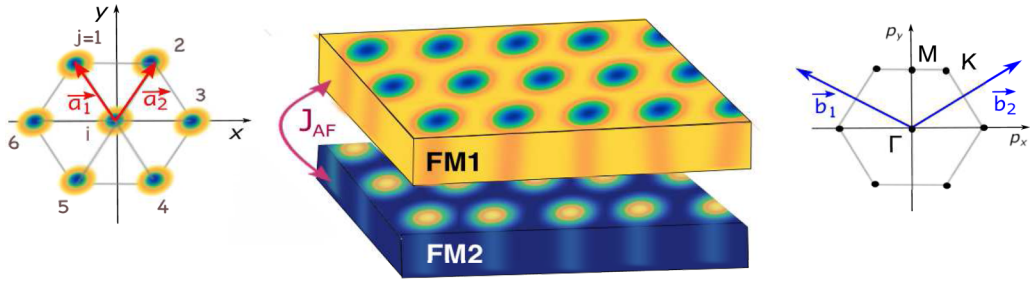


FIG. 1. (a) Schematic of antiferromagnetic skyrmions in a SAF, where two ferromagnetic layers, FM1 and FM2, are coupled *via* an antiferromagnetic interlayer exchange coupling $J_{AF}$. The DM interaction stabilizes the skyrmion structure. Each layer exerts a bias field on the neighboring layer. Skyrmions form a regular triangular lattice (b) with the SkX lattice vectors $\mathbf{a}_1$ and $\mathbf{a}_2$. The SkX lattice parameter is $a_{SkX} = |\mathbf{a}_1| = |\mathbf{a}_2| \equiv r$, where $r$ is the interskyrmion distance. (c) Corresponding Brillouin zone.

generalization of this statement to some long-range interaction models [44]). The system considered in this paper consists of two ferromagnetic layers of a finite (though small) thickness that are coupled antiferromagnetically across a thin nonmagnetic spacing layer. Accordingly, the Mermin-Wagner theorem is not applicable to the system under consideration, and we assume that magnetic order is not destroyed by thermal fluctuations. One should also note that even in the pure 2D case, fluctuations of the order parameter are growing logarithmically at large distances, which makes it possible to neglect this effect in real finite samples.

Based on the free energy given by Eq. (1), one can describe the skyrmion lattice in a ferromagnetic layer as a superposition of three helices [21]. The corresponding low-energy excitations were studied in Refs. [22,25], and a gapless mode of phason excitations with the dispersion quadratic in the wave vector was identified in the absence of pinning. In this representation, the magnetization vector can be parameterized as $\mathbf{m} = m_z\hat{\mathbf{z}} + \sum_{\mu=a,b,c}\mathbf{m}_\mu$, where $m_z$ is a uniform component induced by an external magnetic field, while $\mathbf{m}_\mu$ is the spatial profile of the three helices,

$$\mathbf{m}_\mu = m_h\big(\beta_\mu\hat{\mathbf{k}}_\mu + \sqrt{1-\beta_\mu^2}\,\mathbf{n}_\mu\big), \tag{2}$$

for $\mu = a, b, c$. Here $m_h$ is the helix amplitude and $\boldsymbol{n}_\mu$ represent the helices with wave vectors $\boldsymbol{k}_\mu$,

$$\mathbf{n}_\mu = \hat{\mathbf{z}}\cos(\mathbf{k}_\mu\cdot\mathbf{r}+\varphi_\mu) + (\hat{\mathbf{k}}_\mu\times\hat{\mathbf{z}})\sin(\mathbf{k}_\mu\cdot\mathbf{r}+\varphi_\mu), \tag{3}$$

and $\hat{\mathbf{k}}_\mu$ is a unit vector along $\mathbf{k}_\mu$. One choice of the vectors $\mathbf{k}_\mu$ is $\mathbf{k}_a = k\,(1,0,0)$, $\mathbf{k}_b = k\,(-\frac{1}{2},\frac{\sqrt{3}}{2},0)$, and $\mathbf{k}_c = k\,(-\frac{1}{2},-\frac{\sqrt{3}}{2},0)$. In turn, the three variables $\varphi_\mu$ describe phases of the helices, while $\beta_\mu$ represent massive excitations. The low-energy excitations are described by the phason variables defined as $\varphi_+ \equiv \frac{1}{2}(\varphi_a+\varphi_b)-\varphi_c$ and $\varphi_- \equiv \frac{1}{2\sqrt{3}}(\varphi_a-\varphi_b)$, and the corresponding low-energy Lagrangian was shown to have the form [22]

$$L = \int d^2\mathbf{r}\Big\{g\,(\varphi_+\dot{\varphi}_- - \varphi_-\dot{\varphi}_+) + \frac{m_\varphi}{2}(\dot{\varphi}_+^2+\dot{\varphi}_-^2) - \tilde{A}_{ex}[(\nabla\varphi_+)^2+(\nabla\varphi_-)^2]\Big\}, \tag{4}$$

where $g$ is a constant proportional to the topological charge of the skyrmion, $\tilde{A}_{ex}$ is a constant proportional to the exchange parameter $A_{ex}$, and $m_\varphi \propto 1/(\tilde{A}_{ex}D)$ is a mass term arising from the $\beta_\mu$ modes. Equation (4) leads to the excitation mode which is quadratic in the wave vector $\mathbf{p}$, $\omega(p) \propto \tilde{A}_{ex}p^2$. We note that the description based on Eq. (2) is the simplest approximation, validity of which, however, is confirmed numerically. More general and accurate descriptions are based on elliptical (deformed) spirals and also include higher order harmonics. In this paper, however, we limit the description to helices described by Eq. (2).

The excitation mode becomes significantly changed in the case of two ferromagnetic layers coupled antiferromagnetically. This change appears due to the dynamics of the dominant antiferromagnetic component of the two-layer magnetization. This component experiences fluctuations of the ferromagnetic component of the two layers. We note that this effect is well known for antiferromagnets in general. Let us consider the antiferromagnetic coupling between the two ferromagnetic layers, labeled with the index $i = 1$ (FM1 layer) and $i = 2$ (FM2 layer), see Fig. 1:

$$H_{AF} = J_{AF}\int d^2\mathbf{r}\,(\mathbf{m}_1\cdot\mathbf{m}_2), \tag{5}$$

where $J_{AF}$ is the interlayer coupling constant. Defining the antiferromagnetic moment $\mathbf{n}$ and the ferromagnetic moment $\boldsymbol{\ell}$ as

$$\mathbf{m}_1/M_s = \boldsymbol{n}+\boldsymbol{\ell}, \quad \mathbf{m}_2/M_s = -\mathbf{n}+\boldsymbol{\ell}, \tag{6}$$

the antiferromagnetic coupling can be rewritten as $H_{AF} = J_{AF}\int d^2\mathbf{r}\,(-\mathbf{n}^2+\boldsymbol{\ell}^2)$. The spin dynamics of the system is described by the spin Berry's phase term in the Lagrangian, $L_\mathrm{B} = M_s\int d^2\mathbf{r}\sum_{i=1,2}\cos\theta_i\,\dot{\phi}_i$, written in terms of polar coordinates. Defining $\tilde{\mathbf{m}}_2 \equiv -\mathbf{m}_2$ (with polar coordinates $\tilde{\theta}_2, \tilde{\phi}_2$), this term may be written as $L_\mathrm{B} = M_s\int d^2\mathbf{r}\,(\cos\theta_1\,\dot{\phi}_1 - \cos\tilde{\theta}_2\,\dot{\tilde{\phi}}_2)$, which reduces to $L_\mathrm{B} = M_s\int d^2\mathbf{r}\,\delta\mathbf{m}\cdot(\mathbf{m}_1\times\dot{\mathbf{m}}_1)$ in the lowest order in $\delta\mathbf{m} \equiv \mathbf{m}_1 - \tilde{\mathbf{m}}_2$. The spin Berry's phase term, expressed by $\mathbf{n}$ and $\boldsymbol{\ell}$ (assuming small $\ell$, i.e., large $J_{AF}$), then reads

$$L_\mathrm{B} = -2M_s\int d^2\mathbf{r}\,\boldsymbol{\ell}\cdot(\mathbf{n}\times\dot{\mathbf{n}}), \tag{7}$$

instead of the topological term for the case of a single layer (Eq. (22) of Ref. [22]). By integrating out the $\boldsymbol{\ell}$ variable and neglecting the spatial derivatives of $\boldsymbol{\ell}$, one obtains the kinetic term for $\boldsymbol{n}$:

$$L_\mathrm{B} = \frac{M_s^2}{J_{AF}}\int d^2\mathbf{r}\,\dot{\mathbf{n}}^2. \tag{8}$$

Using $\int d^2\mathbf{r}\,\dot{\mathbf{n}}^2 = \int d^2\mathbf{r}\sum_\mu(\dot{\varphi}_\mu^2 + \dot{\beta}_\mu^2)$, the phason kinetic part of the Lagrangian is

$$L_{\rm B} = \frac{M_s^2}{3J_{AF}}\int d^2\mathbf{r}\,(\dot{\varphi}_+^2 + \dot{\varphi}_-^2), \tag{9}$$

and the total phason Lagrangian for the SAF, without the topological term of a single layer [Eq. (4)], can be written as

$$L = \int d^2\mathbf{r}\left\{\frac{\tilde{m}_\varphi}{2}(\dot{\varphi}_+^2 + \dot{\varphi}_-^2) - \tilde{A}_{ex}[(\nabla\varphi_+)^2 + (\nabla\varphi_-)^2]\right\}, \tag{10}$$

where $\tilde{m}_\varphi \equiv m_\varphi + \frac{2M_s^2}{3J_{AF}}$. The phason dispersion derived from this Lagrangian is massless and linear, $\omega(p) \propto \tilde{A}_{ex}p$, in the absence of pinning. Micromagnetic simulations (Sec. III) support the result of the gapless linear mode.

Applying an ac magnetic field along the in-plane direction, one can pump spin current into the substrate layer. The pumped current is proportional to $\mathbf{m}\times\dot{\mathbf{m}}$ in the phason picture. As discussed in Ref. [22] [Eq. (65)], the in-plane field couples to the massive excitation modes, $\beta_\mu$, and not directly to the phason variables. Thus one can write $\dot{\mathbf{m}}_\mu = m_{\rm h}\dot{\beta}_\mu\hat{\mathbf{k}}_\mu$. After averaging over space, the oscillating components vanish and one obtains $\mathbf{m}\times\dot{\mathbf{m}} = \sum_{\mu\mu'}\mathbf{m}_\mu\times\dot{\mathbf{m}}_{\mu'} = m_{\rm h}^2\sum_{\mu\mu'}(\hat{\mathbf{k}}_\mu\times\hat{\mathbf{k}}_{\mu'})\beta_\mu\dot{\beta}_{\mu'}$. As $(\hat{\mathbf{k}}_\mu\times\hat{\mathbf{k}}_{\mu'})\parallel\hat{\mathbf{z}}$ for $\mu\neq\mu'$, the pumped spin current is polarized along the $z$ direction. The spatial correlation of the $\beta$ modes is determined by both gapless and gapful modes, $\omega^{\pm}(p)$, with the energies $\omega^-(p)\propto p^2$ and $\omega^+(p)\simeq A_{ex}Q^2 + O(p^2)$ (Eq. (66) of Ref. [22]). The correlation length of the pumping is determined by the Gilbert damping constant.

## III. MICROMAGNETIC SIMULATIONS

The skyrmion generation and its collective dynamics in a SAF is governed by the Landau-Lifshitz-Gilbert (LLG) equation,

$$\frac{\partial\mathbf{M}_i}{\partial t} = -\gamma\mathbf{M}_i\times\mathbf{H}_{{\rm eff},i} + \frac{\alpha}{M_{s,i}}\mathbf{M}_i\times\frac{\partial\mathbf{M}_i}{\partial t}, \tag{11}$$

for the top ($i=1$) and bottom ($i=2$) ferromagnetic layers in the SAF. Here, $\mathbf{M}_i = M_s\mathbf{m}_i$ ($M_s$ denotes the saturation magnetization), and $\alpha$ is the phenomenological Gilbert damping constant. The total effective field $\mathbf{H}_{eff,i}$ exerted on the $i$th layer reads $\mathbf{H}_{eff,i} = -\frac{\delta F_{SkX}}{\delta\mathbf{m}_i} - \mathbf{H}_{couple,i}$, where $F_{SkX}$ is given by Eq. (1), $\mathbf{H}_{couple,i} = \frac{J_{AF}}{\mu_0 M_{s,i}t_i}\mathbf{M}_j$ is the bias field exerted by the second layer, $t_i$ is the $i$th-layer thickness, and $j\neq i$. The influence of the out-of-plane magnetic anisotropy and dipole-dipole interaction is not taken into account in the present description.

In numerical calculations we assume the following parameters: $A_{ex} = 10$ pJ/m, $D_m = 0.2$ mJ/m$^2$, $M_s = 1.2$ A/m, $J_{AF} = 0.23$ mJ/m$^2$, and ferromagnetic layer thickness $t_p = 3$ nm. The bias magnetic field $H_z = 100$ mT is used for stabilization of the skyrmion structure. The size of the ferromagnetic layers is $6000\times120\times3$ nm$^3$, which is discretized by the cell size $3\times3\times3$ nm$^3$.

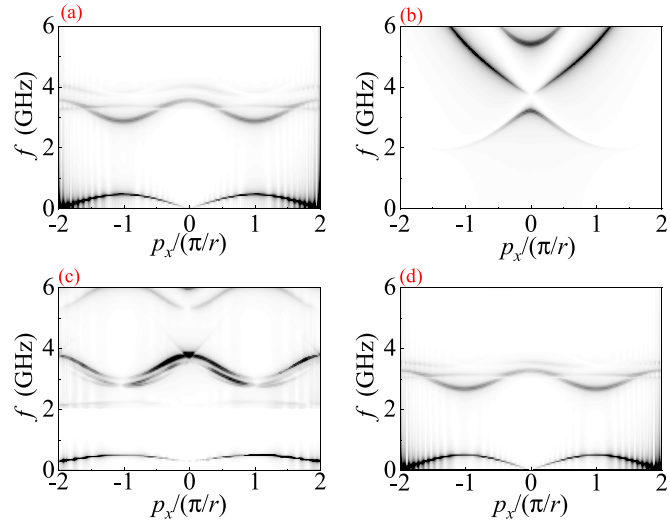


FIG. 2. (a) Low-temperature spectrum of magnetic oscillations in the single ferromagnetic layer with one-dimensional skyrmion lattice. (b) The corresponding spectrum in the absence of skyrmions. (c) The same as in (a) for the external magnetic field field $-20$ mT applied near the skyrmion center (radius of this range is 15 nm). (d) The same as in (a) but for nonzero Ginzburg-Landau parameters, $a_m = 1\times10^5$ J/m$^3$ and $b_m = 5\times10^4$ J/m$^3$. These parameters describe the spin-wave spectrum in the vicinity of Curie temperature. General features of the spectrum are similar to those in (a), except the frequencies are in general slightly smaller. The frequency $f = \omega/(2\pi)$ is shown as a function of $p_x$, and the period of 1D SkX is $r = 61.8$ nm. The Brillouin zone boundaries in (a), (c), (d) are given by $p_x = \pm n\pi/r$.

### A. Single ferromagnetic layer

For clarity reasons, we analyze first the skyrmion dynamics in a single magnetic layer, where the theory based on the model of coupled helices predicts gapless excitations. For simplicity we focus here on the excitations in a one-dimensional SkX. The corresponding low-temperature spectrum of magnetization dynamics is presented in Fig. 2(a), where the frequency $\omega/(2\pi)$ is shown as a function of $p_x$. The periodicity of the SkX, with the period $r$ ($r$ is the distance between skyrmions), is clearly visible in the corresponding band structure, see Fig. 2(a). The gapless excitations near $p_x = 0$ correspond to the collective SkX mode, already discussed above. To emphasize the gapless character of the collective phason excitations, we also calculated the excitation spectrum in the magnetic layer without the SkX, where the excitations are gapped, see Fig. 2(b). The spectrum of magnetic excitations for temperatures close to the Curie temperature is described by specific nonzero values of the Ginzburg-Landau parameters, see Fig. 2(d). These parameters are related to the system's temperature and Curie temperature; for details see Ref. [21] and the corresponding Supplemental Material. The corresponding spectrum is qualitatively similar to that in Fig. 2(a), except the corresponding frequencies are slightly smaller; compare Figs. 2(a) and 2(d). However, when confining the skyrmions through a pinning potential, this mode shifts upward, see Fig. 2(c). All these results show that the micromagnetic calculations lead to the results, which are

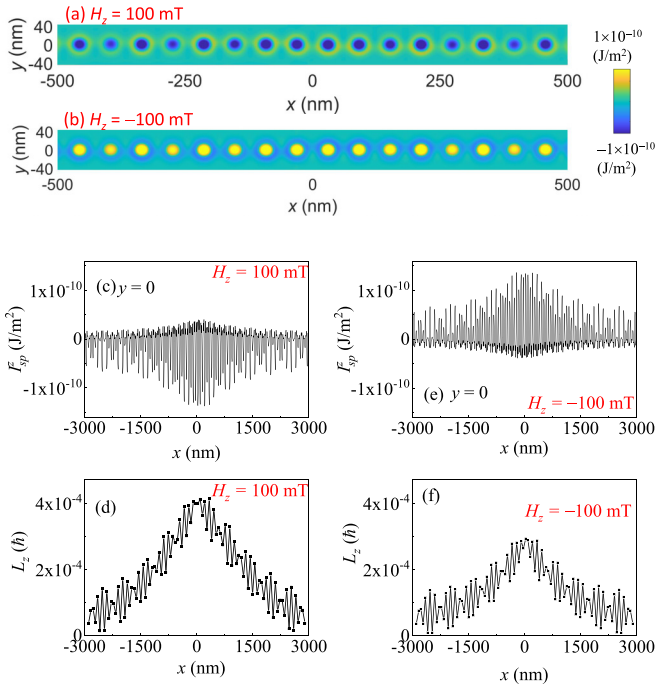


FIG. 3. Micromagnetic simulation for a single layer with 1D skyrmion lattice, stabilized by an applied external magnetic field $H_z = 100\,\mathrm{mT}$ (a) and $H_z = -100\,\mathrm{mT}$ (b). (c), (e) The spatial profiles of the $z$ component of spin pumping current $I_{sp}^z(x, y = 0)$, excited by a microwave field (applied near the region $x = 0$) with the frequency 0.3 GHz. The spin pumping currents in the skyrmion center and at its boundary are opposite. This follows from the magnetic structure of the skyrmion—the magnetization in the skyrmion center is opposite to that at its boundary. (d), (f) The $z$ component of the orbital angular momentum $L_z$ of skyrmions due to phason excitations (the points correspond to the centers of skyrmions).

qualitatively consistent with those obtained in the model based on three coupled helices.

The collective phason excitations of the SkX can pump magnonic spin current $\mathbf{I}_{sp}$ into the adjacent metal. To calculate the pumped spin current we exploit the formula $\mathbf{I}_{sp} = \frac{\hbar g_r}{4\pi}\mathbf{M} \times \frac{\partial \mathbf{M}}{\partial t}$ (where $g_r$ is the real part of the dimensionless spin-mixing conductance, assumed $g_r = 7 \times 10^{18}\ \mathrm{m}^{-2}$) and excite the phason mode with the low-frequency, equal to 0.3 GHz, microwave field applied in the vicinity of the region $x = 0$. The spatial profile of the $z$ component of the magnonic spin pumping current $I_{sp}^z$ is shown in Fig. 3(a) for positive magnetic field and in the corresponding cross section at $y = 0$ in Fig. 3(c). The negative pumping current is mainly localized inside the skyrmion lattice and propagates away from the excitation region ($x = 0$). Outside the skyrmion region, the current $I_{sp}^z$ becomes positive. In the absence of SkX, the magnetization oscillation with frequency 0.3 GHz cannot propagate through the magnetic layer due to the energy gap in the spectrum and therefore the pumping current disappears. When reversing the direction of applied magnetic field, $H_z = -100\,\mathrm{mT}$, and also of the magnetization direction, then the spin current $I_{sp}^z$ also changes its orientation as shown in Figs. 3(b) and 3(e).

The collective phason excitations in the SkX carry an orbital angular momentum created by the dynamics of the

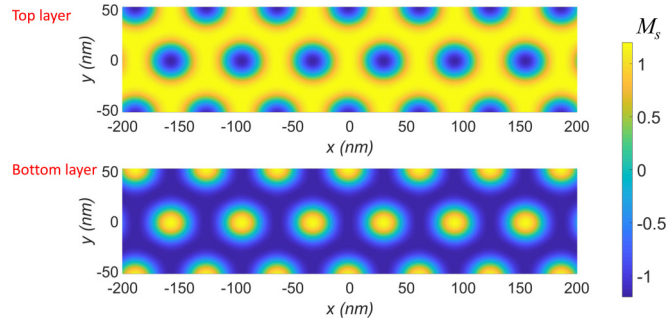


FIG. 4. Schematics of the two-dimensional antiferromagnetic of the SkX in a SAF. Both top and bottom layers are shown.

three coupled helices. The $z$ component of the orbital angular momentum can be calculated using Noether's theorem [45,46] as $L_z = (\hbar/S)\int l_z(x, y)\,dx\,dy$, where $l_z(x, y) = m_z(\mathbf{r} \times \nabla\phi)_z$ is the orbital angular momentum density, $S$ is the integration area, and $\phi = \arctan(m_y/m_x)$. The results of the calculations are shown in Figs. 3(d) and 3(f). Contrary to the magnonic spin pumping current, the orbital angular momentum density does not change sign upon the magnetic field reversal ($H_z = \pm 100\,\mathrm{mT}$). We note that the orbital angular momentum of the phason modes in the SkX can be expressed in terms of the pseudo-Poynting vector [47] as follows: $\mathbf{L} = (1/S)\int \mathbf{r} \times \mathbf{P}\,dxdy$, where $P_\mu = \frac{\hbar}{2}\{\tilde{E}^*(\partial_\mu \tilde{B}) + \tilde{B}^*(\partial_\mu \tilde{E})\}$, and we introduced the notations $\tilde{E} = m_x + im_y$ and $\tilde{B} = i(m_x - im_y)$. The magnon attenuation effect leads to the spatial decay of $L_z$. Therefore, when rescaling the orbital angular momentum dividing it by the magnon density $n$, one can eliminate the effect of spatial decay and achieve the quantized value of $L_z/n$, $L_z/n \approx \hbar$.

### B. The SkX in a SAF

Finally, we consider the skyrmion lattice (one and two dimensions, 1D and 2D, respectively) in a SAF. The corresponding magnetization profile in the 2D case is plotted in Fig. 4. The numerical results on the magnetic dynamics in SAF are compared in Fig. 5 with those for a single magnetic layer. Both the one- and two-dimensional cases are shown there. The dispersion curves in the low-frequency regime in the 1D SkX are linear in both single layer and the SAF. In turn, for 2D SkX, the dispersion curve is still linear in the SAF but becomes quadratic in the single layer. These results are consistent with those obtained in Sec. II for 2D systems within the model based on three coupled helices. Moreover, they are also consistent with those obtained from Thiele's equations, as will be discussed later. The differences between the dispersion curves of 1D and 2D cases (especially for a single layer) originate from different boundary conditions. For a 1D skyrmion lattice, we adopt a finite geo-boundary in the numerical calculations, and the boundary effect blocks one of the degrees the freedom. This blocking is irrelevant in the 2D case, where the periodic boundary conditions are employed.

The spin pumping current $I_{sp}^z$ in the 1D SkX in a SAF is shown in Fig. 6. The bias field of 20 mT is applied near the skyrmion centers in both the top and bottom layers. This field plays the role of a pinning potential that shifts the spectrum

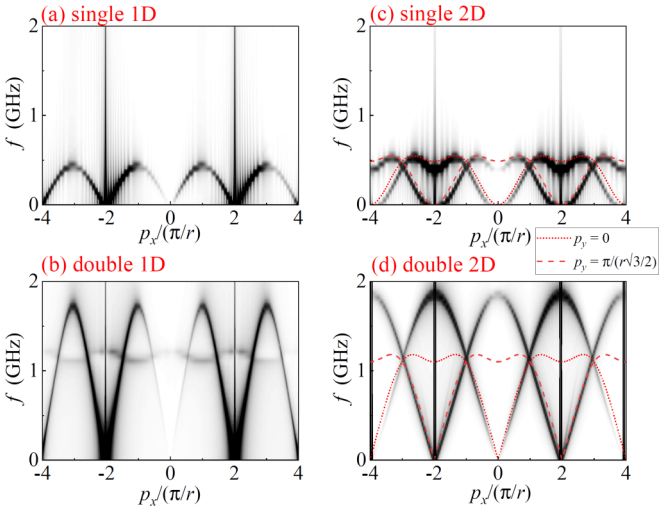


FIG. 5. The spectrum of magnetic excitations in the low-frequency regime plotted for the single ferromagnetic layer (a), (c) and for the SAF (b), (d). The corresponding skyrmion lattices are 1D (a), (b) and 2D (c), (d). The red dotted ($q_y = 0$) and dashed $[q_y/(\pi/r) = 2/\sqrt{3}]$ lines are calculated using Eqs. (26) and (40), respectively, for $\sigma = 0.06$ GHz and $\sigma_{12} = 1$ GHz.

of the system upward [Fig. 6(a)]. By applying the microwave field in the vicinity of $x = 0$ in the top layer of SAF, one can induce the skyrmion precession in both layers of the SAF. The skyrmion precession in the top layer generates the negative spin pumping current $I^z_{sp}$ shown in blue color in Fig. 6(b). Due to the antiferromagnetic (AFM) coupling, magnetization dynamics in both layers are correlated, and spin pumping current in the bottom layer is also negative. However, the skyrmion precession and the magnitude of the current are smaller as compared to those in the top layer. The negative $I^z_{sp}$ in the SAF is similar to the skyrmion precession and spin pumping current generated in a single layer Fig. 3(a). The microwave field applied to the bottom layer Fig. 6(d) generates the skyrmion precession and positive spin pumping current $I^z_{sp}$ (shown in yellow). The effect is similar to the single-layer case Fig. 3(b). Due to the AFM coupling with a top layer, the spin pumping current in the top layer $I^z_{sp}$ is also positive, but the current is smaller than that in the bottom layer.

The interesting feature is the spatially nonuniform distribution of the current. In particular, from Fig. 6(b) it follows that at a certain distance from the $x = 0$ point, the spin pumping current $I^z_{sp}$ becomes positive, while at larger distances it again switches sign. Thus we observe a spatially periodic switching of the sign of current $I^z_{sp}$. The spatial distribution of the current also depends on the frequency of the field, Fig. 6(c). The skyrmion precession in the bottom layer, Fig. 6(d), switches the sign of current $I^z_{sp}$ in both layers as compared with Fig. 6(b).

The spatial alternation of the magnonic current can be explained as follows: Due to the antiferromagnetic coupling, both left-hand and right-hand precessions (concerning the local magnetization) coexist in the SAF. For the skyrmion with negative magnetization in the center and positive magnetization at the boundary, the pumping current $I^z_{\rm sp}$ is negative in the center and positive at the boundary. When the current $I^z_{\rm sp}$ reaches the neighboring skyrmion, it becomes negative again

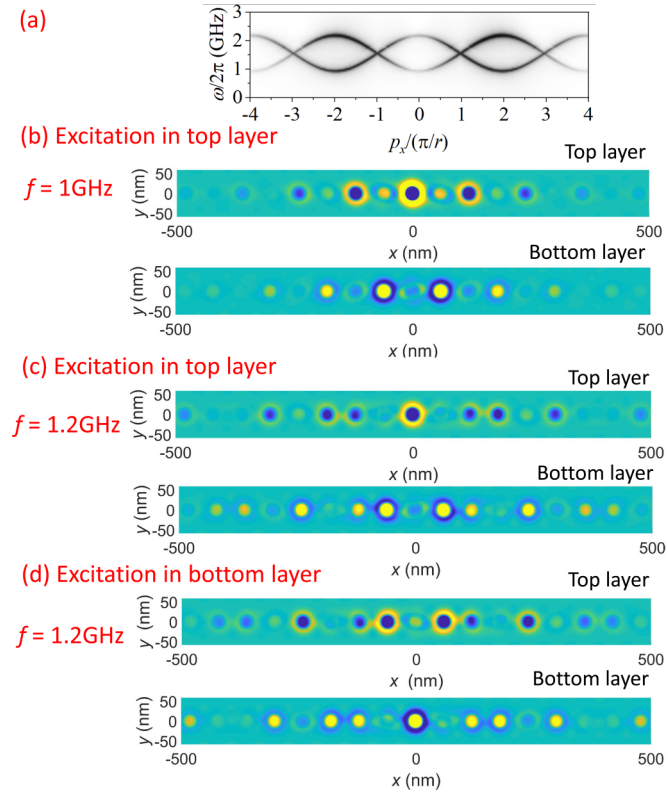


FIG. 6. (a) The spectrum of 1D skyrmion lattice in a SAF when a bias field of 20 mT is applied near the skyrmion centers in both top and bottom layers. (b)–(d) The spatial profiles of the $z$ component of spin pumping current $I^z_{sp}$ in the SAF layer. The spin pumping current and skyrmion precession are excited by the microwave field with frequencies 1 GHz (b) and 1.2 GHz (c). The skyrmion precession is excited in the region $x = 0$ in the top layer. (d) The current $I^z_{sp}$ generated by the skyrmion excitation in the bottom layer. The microwave field is applied in the region $x = 0$.

because the skyrmion permits only right-hand precession. In SAF, due to the coexisting left and right precessions, the current $I^z_{sp}$ can be either positive or negative. However, there is a significant asymmetry—the right-hand precession is always stronger. Therefore, the $-z$ magnetization in the top layer and the right-hand precession induces the negative current, stronger than the negative current induced in the bottom layer due to the left-hand precession and positive $z$ magnetization. In Fig. 6(b) the negative current induced in the top layer leads to a smaller negative current in the bottom layer. The negative current emitted to the border of the first skyrmion changes the sign, and the positive current reaches the region of the second skyrmion. The positive $I^z_{sp} > 0$ generates a stronger positive current in the bottom layer. Then $I^z_{sp}$ again becomes negative in the region of the third skyrmion, and the process is repeated further.

The orbital angular momentum density $L_z$ of the 1D SkX in SAF is plotted in Fig. 7 for two cases: when the microwave field is applied to the top (a) and bottom (b) layers of the SAF. As one can see, when the microwave is applied to the top layer, the orbital angular momentum density in the top layer is larger and vice versa—when the bottom layer is excited by the microwave field, the orbital angular momentum density is larger in the bottom layer.

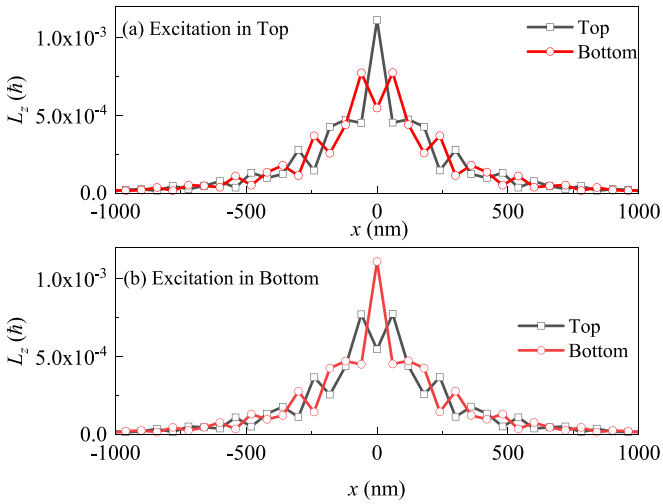


FIG. 7. The $z$ component of the orbital angular momentum $L_z$ calculated for the 1D SkX in a SAF when the oscillation is excited by a microwave field applied near $x = 0$ in the (a) top and (b) bottom layer. The frequency of the field is 1.2 GHz.

## IV. MODEL BASED ON THIELE'S EQUATIONS

In case of skyrmions stabilized by the DM interaction, the center-of-mass motion of an individual skyrmion can be described by Thiele's equation [48],

$$-\mathbf{G}\times\partial_t\mathbf{r}-\alpha\overleftrightarrow{\mathcal{D}}\,\partial_t\mathbf{r}+\mathbf{F}=0, \tag{12}$$

where $\mathbf{G}=4\pi N_{\rm sk}\,\hat{z}$ is the gyrocoupling vector, defined by the skyrmion topological charge $N_{\rm sk}=\pm1$ and the unit vector $\hat{z}$ along the $z$ axis, $\overleftrightarrow{\mathcal{D}}$ stands for a tensor of dissipative force, $\alpha$ is the Gilbert damping constant, and $\mathbf{F}$ is a force acting on the skyrmion ($\mathbf{F}=-\nabla V$, with $V$ standing for the corresponding potential energy). The tensor $\overleftrightarrow{\mathcal{D}}$ has the following form: $\overleftrightarrow{\mathcal{D}}_{ij}=D$ for $(i,j)=(x,x)$ and $(i,j)=(y,y)$, while $\overleftrightarrow{\mathcal{D}}_{ij}=0$ otherwise [49]. This particlelike description of skyrmion dynamics is also valid for systems of interacting skyrmions [49–51].

### A. Single-layer case

We consider first the dynamical states of SkX in a single ferromagnetic layer. To do this we model SkX as a periodic (in equilibrium) array of coupled skyrmions confined in the positions $\mathbf{R}_i$, where each skyrmion is surrounded by six nearest neighbors. In a nonequilibrium (dynamical) state, the position of the $i$th skyrmion, $\mathbf{r}_i$, can written as $\mathbf{r}_i=\mathbf{R}_i+\mathbf{u}_i$, where $\mathbf{u}_i$ stands for a deviation of the skyrmion center from its equilibrium position.

Let us consider two nearest-neighbor interacting skyrmions, $i$ and $j$, located in equilibrium at the positions $\mathbf{R}_i$ and $\mathbf{R}_j$, and let $\mathbf{e}_{ij}$ stand for a unit vector along $\mathbf{R}_j-\mathbf{R}_i$. The energy of such skyrmions in nonequilibrium is generally anisotropic, i.e., it depends on the relative orientation of the skyrmion displacements and the vector $\mathbf{e}_{ij}$. Thus the relative displacement, $\mathbf{u}_i-\mathbf{u}_j$, can be decomposed into the component $[\mathbf{e}_{ij}\cdot(\mathbf{u}_i-\mathbf{u}_j)]\mathbf{e}_{ij}$ along the vector $\mathbf{e}_{ij}$ and the component $(\mathbf{u}_i-\mathbf{u}_j)-[\mathbf{e}_{ij}\cdot(\mathbf{u}_i-\mathbf{u}_j)]\mathbf{e}_{ij}$ normal to $\mathbf{e}_{ij}$.

Since the total force acting on the $i$th skyrmion is a superposition of the forces from its nearest neighbors, we write the Thiele's equation in the following form:

$$\begin{aligned}&-\mathbf{G}\times\partial_t\mathbf{u}_i-\alpha\overleftrightarrow{\mathcal{D}}\,\partial_t\mathbf{u}_i\\&=\sigma_\parallel\sum_{\langle j\rangle}[\mathbf{e}_{ij}\cdot(\mathbf{u}_i-\mathbf{u}_j)]\mathbf{e}_{ij}\\&\quad+\sigma_\perp\sum_{\langle j\rangle}\{(\mathbf{u}_i-\mathbf{u}_j)-[\mathbf{e}_{ij}\cdot(\mathbf{u}_i-\mathbf{u}_j)]\mathbf{e}_{ij}\},\end{aligned} \tag{13}$$

where $\sigma_\parallel$ and $\sigma_\perp$ are the two coupling parameters, and $\langle j\rangle$ denotes the summation over the nearest-neighbor skyrmions. A particular skyrmion (say the $i$th one) is surrounded by six nearest neighbors indexed with $j=1$ to $j=6$. They correspond to $\mathbf{e}_{i1}=(1,0)$, $\mathbf{e}_{i2}=(1/2,\sqrt{3}/2)$, $\mathbf{e}_{i3}=(-1/2,\sqrt{3}/2)$, $\mathbf{e}_{i4}=(-1,0)$, $\mathbf{e}_{i5}=(-1/2,-\sqrt{3}/2)$, and $\mathbf{e}_{i6}=(1/2,-\sqrt{3}/2)$.

In the following we assume skyrmions corresponding to $N_{sk}=1$ and adequately normalize $\overleftrightarrow{\mathcal{D}}$ as well as $\sigma_\parallel$ and $\sigma_\perp$. Taking into account the explicit form of the tensor $\overleftrightarrow{\mathcal{D}}$ [49,51], the Thiele's equations for a skyrmion lattice in a single ferromagnetic layer can be written in the form

$$\begin{aligned}&-\partial_t u_i^y-\alpha\mathcal{D}\,\partial_t u_i^x\\&=\sum_{\langle j\rangle}\left\{\left[\sigma_\parallel e_{ijx}^2+\sigma_\perp\left(1-e_{ijx}^2\right)\right]\right.\\&\quad\left.\times\left(u_i^x-u_j^x\right)+(\sigma_\parallel-\sigma_\perp)e_{ijx}e_{ijy}\left(u_i^y-u_j^y\right)\right\},\end{aligned} \tag{14}$$

$$\begin{aligned}&\partial_t u_i^x-\alpha\mathcal{D}\,\partial_t u_i^y\\&=\sum_{\langle j\rangle}\left\{\left[\sigma_\parallel e_{ijy}^2+\sigma_\perp\left(1-e_{ijy}^2\right)\right]\right.\\&\quad\left.\times\left(u_i^y-u_j^y\right)+(\sigma_\parallel-\sigma_\perp)e_{ijx}e_{ijy}\left(u_i^x-u_j^x\right)\right\}.\end{aligned} \tag{15}$$

We look now for solutions of the above equations in the Bloch's form, $u_i^{x(y)}=u_0^{x(y)}e^{i[\mathbf{p}\cdot\mathbf{R}_i-\omega(t)]}$. For simplicity, we neglect the term proportional to $\mathcal{D}$ as being small due to a small damping parameter $\alpha$. Then, taking into account positions of all six neighbors, one finds from Eqs. (5) and (6) the following equations:

$$\begin{aligned}i\omega u_0^y&=\{2\sigma_\parallel[1-\cos(p_x r)]+(\sigma_\parallel+3\sigma_\perp)[1\\&\quad-f_1(\mathbf{p})]\}u_0^x+\sqrt{3}(\sigma_\parallel-\sigma_\perp)f_2(\mathbf{p})u_0^y,\end{aligned} \tag{16}$$

$$\begin{aligned}-i\omega u_0^x&=\{2\sigma_\perp[1-\cos(p_x r)]+(3\sigma_\parallel+\sigma_\perp)[1\\&\quad-f_1(\mathbf{p})]\}u_0^y+\sqrt{3}(\sigma_\parallel-\sigma_\perp)f_2(\mathbf{p})u_0^x,\end{aligned} \tag{17}$$

where

$$f_1(\mathbf{p})=\cos\left(\frac{p_x r}{2}\right)\cos\left(\frac{\sqrt{3}}{2}p_y r\right), \tag{18}$$

$$f_2(\mathbf{p})=\sin\left(\frac{p_x r}{2}\right)\sin\left(\frac{\sqrt{3}}{2}p_y r\right), \tag{19}$$

and $r$ is the distance between nearest-neighbor skyrmions. Defining the column vector $\mathbf{z} = (u_0^x, u_0^y)^T$, the above equations (16) and (17) can be written as

$$\hat{H}\mathbf{z} = 0, \tag{20}$$

where the $2 \times 2$ matrix $\hat{H}$ has the form

$$\hat{H} = \begin{pmatrix} B & A - i\omega \\ A + i\omega & B' \end{pmatrix}, \tag{21}$$

with

$$A = \sqrt{3}(\sigma_\parallel - \sigma_\perp) f_2(\mathbf{p}), \tag{22}$$

$$B = 2\sigma_\parallel [1 - \cos(p_x r)] + (\sigma_\parallel + 3\sigma_\perp)[1 - f_1(\mathbf{p})], \tag{23}$$

$$B' = 2\sigma_\perp [1 - \cos(p_x r)] + (3\sigma_\parallel + \sigma_\perp)[1 - f_1(\mathbf{p})]. \tag{24}$$

The condition of the vanishing determinant of the matrix $\hat{H}$ leads to the following frequency $\omega$:

$$\begin{aligned}\omega = [&\{2\sigma_\parallel [1 - \cos(p_x r)] + (\sigma_\parallel + 3\sigma_\perp)[1 - f_1(\mathbf{p})]\} \\ &\times \{2\sigma_\perp [1 - \cos(p_x r)] + (3\sigma_\parallel + \sigma_\perp)[1 - f_1(\mathbf{p})]\} \\ &- 3[(\sigma_\parallel - \sigma_\perp) f_2(\mathbf{p})]^2]^{1/2}.\end{aligned} \tag{25}$$

In the limit of small $|\mathbf{p}|$, the frequency can expanded as $\omega \approx \frac{3\sqrt{(3\sigma_\parallel + \sigma_\perp)(\sigma_\parallel + 3\sigma_\perp)}}{8}(pr)^2$.

In the isotropic limit, $\sigma_\parallel = \sigma_\perp = \sigma$, this formula reduces to the following simple expression for the phason frequency $\omega$:

$$\omega = 2\sigma[3 - \xi(\mathbf{p})], \tag{26}$$

where $\xi(\mathbf{p})$ is defined as

$$\xi(\mathbf{p}) = \cos(p_x r) + 2\cos\left(\frac{\sqrt{3}}{2} p_y r\right)\cos\left(\frac{1}{2} p_x r\right). \tag{27}$$

From this formula one can easily note that the spectrum is gapless. Moreover, from expansion with respect to $p$ it follows that the spectrum in the small-wave-vector limit is quadratic in $p$, i.e., $\omega \sim p^2$, as is proved by the series expansion $\omega \approx \frac{3\sigma}{2}(pr)^2$.

### B. Thiele's equations for SAF

Now, we apply the description based on the Thiele's equations to the SkX in SAF. Let the skyrmions in the top (FM1) layer (see Fig. 1) be in the positions $\mathbf{r}_i^{(1)} = \mathbf{R}_i + \mathbf{u}_i^{(1)}$, while in the bottom layer they are in positions $\mathbf{r}_i^{(2)} = \mathbf{R}_i + \mathbf{u}_i^{(2)}$. We assumed here that in equilibrium skyrmions in both layers are in the same positions, $\mathbf{R}_i^{(1)} = \mathbf{R}_i^{(2)} = \mathbf{R}_i$. Accordingly, the Thiele's equations can be written as follows:

$$\begin{aligned}-\mathbf{G}^{(1)} \times \partial_t \mathbf{u}_i^{(1)} - \alpha^{(1)} \overleftrightarrow{\mathcal{D}}^{(1)} \partial_t \mathbf{u}_i^{(1)} = {} & \sigma_{1\parallel} \sum_{\langle j \rangle} \left[\mathbf{e}_{ij} \cdot \left(\mathbf{u}_i^{(1)} - \mathbf{u}_j^{(1)}\right)\right] \mathbf{e}_{ij} + \sigma_{1\perp} \sum_{\langle j \rangle} \left\{\left(\mathbf{u}_i^{(1)} - \mathbf{u}_j^{(1)}\right)\right. \\ & \left. - \left[\mathbf{e}_{ij} \cdot \left(\mathbf{u}_i^{(1)} - \mathbf{u}_j^{(1)}\right)\right] \mathbf{e}_{ij}\right\} + \sigma_{12}\left(\mathbf{u}_i^{(1)} - \mathbf{u}_i^{(2)}\right),\end{aligned} \tag{28}$$

$$\begin{aligned}-\mathbf{G}^{(2)} \times \partial_t \mathbf{u}_i^{(2)} - \alpha^{(2)} \overleftrightarrow{\mathcal{D}}^{(2)} \partial_t \mathbf{u}_i^{(2)} = {} & \sigma_{2\parallel} \sum_{\langle j \rangle} \left[\mathbf{e}_{ij} \cdot \left(\mathbf{u}_i^{(2)} - \mathbf{u}_j^{(2)}\right)\right] \mathbf{e}_{ij} + \sigma_{2\perp} \sum_{\langle j \rangle} \left\{\left(\mathbf{u}_i^{(2)} - \mathbf{u}_j^{(2)}\right)\right. \\ & \left. - \left[\mathbf{e}_{ij} \cdot \left(\mathbf{u}_i^{(2)} - \mathbf{u}_j^{(2)}\right)\right] \mathbf{e}_{ij}\right\} + \sigma_{12}\left(\mathbf{u}_i^{(2)} - \mathbf{u}_i^{(1)}\right),\end{aligned} \tag{29}$$

where the in-plane coupling constants in the top (bottom) layer are $\sigma_{1\parallel}$ and $\sigma_{1\perp}$ ($\sigma_{2\parallel}$ and $\sigma_{2\perp}$), whereas $\sigma_{12}$ denotes the coupling parameter between skyrmions in different layers. (Each skyrmion in one layer has only a single nearest-neighbor skyrmion in the second layer.) Note that the coupling between skyrmions in two different layers is isotropic. Other parameters in the two layers are distinguished with the upper indices (1) and (2).

Due to antiferromagnetic interlayer coupling between layers, the magnetic texture in the ferromagnetic layer FM2 is topologically reversed to that in the layer FM1, and consequently, topological charges of skyrmions in these layers are also opposite, $N_{\rm sk}^{(2)} = -N_{\rm sk}^{(1)}$. Accordingly, the Thiele's equations can be written explicitly as follows:

$$\begin{aligned}-\partial_t u_{iy}^{(1)} - \alpha^{(1)} \mathcal{D}^{(1)} \partial_t u_{ix}^{(1)} = {} & \sum_{\langle j \rangle} \left\{\left[\sigma_{1\parallel} e_{ijx}^2 + \sigma_{1\perp}\left(1 - e_{ijx}^2\right)\right]\left(u_{ix}^{(1)} - u_{jx}^{(1)}\right)\right. \\ & \left. + (\sigma_{1\parallel} - \sigma_{1\perp}) e_{ijx} e_{ijy}\left(u_{iy}^{(1)} - u_{jy}^{(1)}\right)\right\} + \sigma_{12}\left(u_{ix}^{(1)} - u_{ix}^{(2)}\right),\end{aligned} \tag{30}$$

$$\begin{aligned}\partial_t u_{ix}^{(1)} - \alpha^{(1)} \mathcal{D}^{(1)} \partial_t u_{iy}^{(1)} = {} & \sum_{\langle j \rangle} \left\{\left[\sigma_{1\parallel} e_{ijy}^2 + \sigma_{\perp}\left(1 - e_{ijy}^2\right)\right]\left(u_{iy}^{(1)} - u_{jy}^{(1)}\right)\right. \\ & \left. + (\sigma_{1\parallel} - \sigma_{1\perp}) e_{ijx} e_{ijy}\left(u_{ix}^{(1)} - u_{jx}^{(1)}\right)\right\} + \sigma_{12}\left(u_{iy}^{(1)} - u_{iy}^{(2)}\right),\end{aligned} \tag{31}$$

$$\begin{aligned}+\partial_t u_{iy}^{(2)} - \alpha^{(2)} \mathcal{D}^{(2)} \partial_t u_{ix}^{(2)} = {} & \sum_{\langle j \rangle} \left\{\left[\sigma_{2\parallel} e_{ijx}^2 + \sigma_{2\perp}\left(1 - e_{ijx}^2\right)\right]\left(u_{ix}^{(2)} - u_{jx}^{(2)}\right)\right. \\ & \left. + (\sigma_{2\parallel} - \sigma_{2\perp}) e_{ijx} e_{ijy}\left(u_{iy}^{(2)} - u_{jy}^{(2)}\right)\right\} + \sigma_{12}\left(u_{ix}^{(2)} - u_{ix}^{(1)}\right),\end{aligned} \tag{32}$$

$$-\partial_t u_{ix}^{(2)} - \alpha^{(2)}\mathcal{D}^{(2)}\,\partial_t u_{iy}^{(2)} = \sum_{\langle j\rangle}\Big\{\big[\sigma_{2\parallel}e_{ijy}^2 + \sigma_{2\perp}\big(1-e_{ijy}^2\big)\big]\big(u_{iy}^{(2)} - u_{jy}^{(2)}\big) + (\sigma_{2\parallel}-\sigma_{2\perp})e_{ijx}e_{ijy}\big(u_{ix}^{(2)} - u_{jx}^{(2)}\big)\Big\} + \sigma_{12}\big(u_{iy}^{(2)} - u_{iy}^{(1)}\big). \tag{33}$$

Similarly, as in the single-layer case, we neglect the term proportional to $\mathcal{D}$ and look for solutions of the above equations in the Bloch's wave form, $u_i^{x(y)} = u_0^{x(y)}e^{i[\mathbf{p}\cdot\mathbf{R}_i-\omega(t)]}$. Then, taking into account positions of all six in-plane nearest neighbors, from Eqs. (30)–(33) one finds

$$i\omega u_0^{(1)y} = \{2\sigma_{1\parallel}[1-\cos(p_x r)] + (\sigma_{1\parallel}+3\sigma_{1\perp})[1-f_1(\mathbf{p})]\}u_0^{(1)x} + \sqrt{3}(\sigma_{1\parallel}-\sigma_{1\perp})f_2(\mathbf{p})u_0^{(1)y} + \sigma_{12}\big[u_0^{(1)x} - u_0^{(2)x}\big], \tag{34}$$

$$-i\omega u_0^{(1)x} = \{2\sigma_{1\perp}[1-\cos(p_x r)] + (3\sigma_{1\parallel}+\sigma_{1\perp})[1-f_1(\mathbf{p})]\}u_0^{(1)y} + \sqrt{3}(\sigma_{1\parallel}-\sigma_{1\perp})f_2(\mathbf{p})u_0^{(1)x} + \sigma_{12}\big[u_0^{(1)y} - u_0^{(2)y}\big], \tag{35}$$

and

$$-i\omega u_0^{(2)y} = \{2\sigma_{2\parallel}[1-\cos(p_x r)] + (\sigma_{2\parallel}+3\sigma_{2\perp})[1-f_1(\mathbf{p})]\}u_0^{(2)x} + \sqrt{3}(\sigma_{2\parallel}-\sigma_{2\perp})f_2(\mathbf{p})u_0^{(2)y} + \sigma_{12}\big[u_0^{(2)x} - u_0^{(1)x}\big], \tag{36}$$

$$i\omega u_0^{(2)x} = \{2\sigma_{2\perp}[1-\cos(p_x r)] + (3\sigma_{2\parallel}+\sigma_{2\perp})[1-f_1(\mathbf{p})]\}u_0^{(2)y} + \sqrt{3}(\sigma_{2\parallel}-\sigma_{2\perp})f_2(\mathbf{p})u_0^{(2)x} + \sigma_{12}\big[u_0^{(2)y} - u_0^{(1)y}\big]. \tag{37}$$

Similarly, as in the case of single layer, we define the column vector $\mathbf{z} = (u_0^{(1)x}, u_0^{(1)y}, (u_0^{(2)x}, u_0^{(2)y})^T$. Then the above equations (34)–(37) can be written as

$$\hat{\tilde{H}}\mathbf{z} = 0. \tag{38}$$

Here the $4\times 4$ matrix $\hat{\tilde{H}}$ takes the form

$$\hat{\tilde{H}} = \begin{pmatrix} \hat{H}^{(1)} + \sigma_{12}\hat{I} & -\sigma_{12}\hat{I} \\ -\sigma_{12}\hat{I} & \hat{H}^{(2)*} + \sigma_{12}\hat{I} \end{pmatrix}, \tag{39}$$

where $\hat{H}^{(1)}$ and $\hat{H}^{(2)}$ are the matrices $\hat{H}$ [see Eq. (21)] corresponding to the top and bottom layers, respectively, while $\hat{I}$ is the $2\times 2$ unit matrix. Frequency can be determined numerically from the condition of the vanishing determinant of the matrix $\hat{\tilde{H}}$ [Eq. (39)].

In the isotropic and symmetric case, $\sigma_{1\parallel} = \sigma_{1\perp} = \sigma_{2\parallel} = \sigma_{2\perp} = \sigma$, one can find the following simple analytical formula for the phason frequency:

$$\omega_\pm = \pm 2\sqrt{(3-\xi(\mathbf{p}))\sigma[(3-\xi(\mathbf{p}))\sigma + \sigma_{12}]}, \tag{40}$$

where $\xi(\mathbf{p})$ is defined by Eq. (27). We note that the positive (negative) frequency corresponds to the right-hand (left-hand) precession of the skyrmions in SAF, and the negative mode is opposite to the positive one, $\omega_-(\mathbf{p}) = -\omega_+(\mathbf{p})$. Importantly, as follows from series expansion, the mode in SAF then becomes linear with $\mathbf{p}$ in the limit of small $|\mathbf{p}|$, $\omega_\pm \sim \pm p$. This is proved by the small $|\mathbf{p}|$ expansion, $\omega_\pm \approx \pm\sqrt{3\sigma\sigma_{12}}pr$. This linear-in-$|\mathbf{p}|$ dependence of the excitation frequency in SAF is much more evident when $\sigma_{12} \gg \sigma$ [Figs. 8(e) and 8(f)]. Such a situation seems to be physically more likely, as the in-plane skyrmion lattice constant is much larger than the thickness of the nonmagnetic spacer layer in SAF.

In Fig. 8 we present numerical results on the dispersion curves of the phason modes propagating in a single ferromagnetic layer as well as in a symmetric ($\sigma_{1\parallel} = \sigma_{2\parallel} = \sigma_\parallel$ and $\sigma_{1\perp} = \sigma_{2\perp} = \sigma_\perp$) SAF. We also distinguish between isotropic ($\sigma_\parallel = \sigma_\perp$) and anisotropic ($\sigma_\parallel > \sigma_\perp$) situations. When the coupling between skyrmions across the spacer layer is weak, $\sigma_{12} \ll \sigma$, the dispersion relation for a SAF is very similar to that found in the single ferromagnetic layer [Figs. 8(a) and 8(b)]. However, when the interlayer coupling between the skyrmions is comparable to or stronger than the intralayer one, $\sigma_{12} \simeq \sigma$, the mode in the SAF is significantly different from that for a single layer [Figs. 8(c) and 8(d)]. The frequency of phason excitations also depends on the coupling anisotropy and becomes reduced when $\sigma_\perp$ becomes smaller than $\sigma_\parallel$

The results derived from the Thiele's equations are in agreement with those obtained from numerical simulations for 2D SkXs. This is shown in Figs. 5(c) and 5(d), where we have added the results obtained from the Thiele's, see the red dotted and dashed lines. The agrement between analytical results derived from the Thiele's equations and those obtained from numerical simulations is satisfactory, confirming that the low-energy spectrum in a single SkX layer is quadratic while the spectrum of 2D SkX in SAF is linear.

## V. SUMMARY AND CONCLUSIONS

In summary, we studied phason excitations of a skyrmion lattice in synthetic antiferromagnets, i.e., in two ferromagnetic layers coupled antiferromagnetically due to interlayer exchange interaction. We have considered the magnetic dynamics of a skyrmion lattice in a SAF. Three different methods have been used to analyze the spectrum of magnetic dynamics: (i) an analytical approach based on the presentation of the SkX as a superposition of three helices, (ii) numerical micromagnetic simulations, and (iii) a simplified approach based on the Thiele's equations. Interestingly, all the three approaches give consistent results, i.e., all lead to gapless and linear phason modes.

For comparison, we have also analyzed 1D and 2D single-layer skyrmion lattices. In the 2D case we found gapless modes with quadratic dispersion in the small-wave-vector limit. In turn, in the 1D case the situation is different, and we found linear behavior (except the approach based on the Thiele's equation, where this behavior is quadratic).

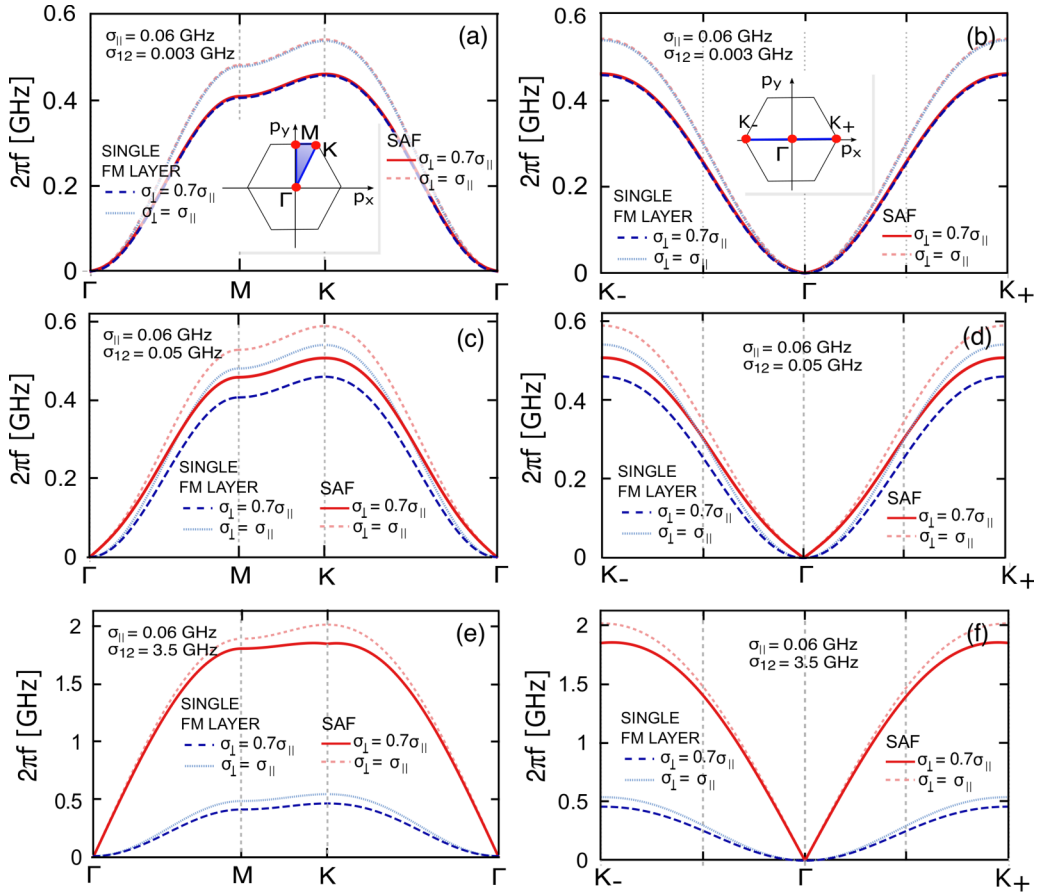


FIG. 8. Dispersion relations of the phason excitations in 2D within the approach based on Thiele's equation, plotted along the main crystal directions in the Brillouin zone of SkX. The dotted line corresponds to the modes in a single ferromagnetic layer, while the solid line presents the positive mode, $\omega_+(\mathbf{p})$, in a SAF. The negative mode in the SAF is exactly opposite to the positive one, $\omega_-(\mathbf{p}) = -\omega_+(\mathbf{p})$, so it is not presented in the figure. The red curves correspond to a symmetric SAF ($\sigma_{1\parallel} = \sigma_{2\parallel} = \sigma_\parallel$ and $\sigma_{1\perp} = \sigma_{2\perp} = \sigma_\perp$) while the blue ones to a single layer. For each case two situations are distinguished: isotropic ($\sigma_\parallel = \sigma_\perp$) and anisotropic ($\sigma_\parallel > \sigma_\perp$). Different panels correspond to the following situations: (a), (b) $\sigma_{12} \ll \sigma_\parallel$; (c), (d) $\sigma_{12} \approx \sigma_\parallel$; and (e), (f) $\sigma_{12} \gg \sigma_\parallel$.

We have also analyzed numerically the spin current pumped by skyrmion dynamics (phasons). Spatial variation of the pumped current polarization is shown to reveal the internal magnetic texture of the skyrmions. In addition, orbital angular momentum associated with phason dynamics induced externally by a microwave field has also been calculated.

We found that three independent helix modes hosted in the synthetic antiferromagnetic material possess beneficial features for generation of magnonic spin currents and implementation in spin caloritronics.

## ACKNOWLEDGMENTS

This work was supported by the National Science Center in Poland by Norwegian Financial Mechanism No. 2014-2021 under the Polish-Norwegian Research Project NCN GRIEG (2Dtronics) No. 2019/34/H/ST3/00515 (A.D., J.B.) and as Research Project No. DEC-2017/27/B/ST3/02881 (V.K.D.). It was also supported by the DFG through the SFB-TRR 227, Shota Rustaveli National Science Foundation of Georgia (SRNSFG) (Grant No. FR-19-4049), the National Natural Science Foundation of China (Grants No. 12174452, No. 12074437, and No. 11704415), the Natural Science Foundation of Hunan Province of China (Grants No. 2022JJ20050 and No. 2021JJ30784), and Grant-in-Aid for Scientific Research (B) (No. 17H02929) from the Japan Society for the Promotion of Science. A.E. acknowledges financial support from the DFG through priority program SPP1666 (Topological Insulators), SFB-TRR227, and OeAD Grants No. HR 07/2018 and No. PL 03/2018. A.E. acknowledges the funding by the Fonds zur Förderung der Wissenschaftlichen Forschung (FWF) under Grant No. I 5384.

[1] B. Barton-Singer, C. Ross, and B. J. Schroers, Commun. Math. Phys. **375**, 2259 (2020).

[2] B. J. Schroers, Phys. Lett. B **356**, 291 (1995).

[3] S. Seki, X. Yu, S. Ishiwata, and Y. Tokura, Science **336**, 198 (2012).

[4] M. N. Wilson, A. B. Butenko, A. N. Bogdanov, and T. L. Monchesky, Phys. Rev. B **89**, 094411 (2014).

[5] J. S. White, K. Prša, P. Huang, A. A. Omrani, I. Živković, M. Bartkowiak, H. Berger, A. Magrez, J. L. Gavilano, G. Nagy, J. Zang, and H. M. Ronnow, Phys. Rev. Lett. **113**, 107203 (2014).

[6] A. Derras-Chouk, E. M. Chudnovsky, and D. A. Garanin, Phys. Rev. B **98**, 024423 (2018).

[7] S. Haldar, S. von Malottki, S. Meyer, P. F. Bessarab, and S. Heinze, Phys. Rev. B **98**, 060413(R) (2018).

[8] A. O. Leonov and M. Mostovoy, Nat. Commun. **6**, 8275 (2015).

[9] C. Psaroudaki, S. Hoffman, J. Klinovaja, and D. Loss, Phys. Rev. X **7**, 041045 (2017).

[10] K. A. van Hoogdalem, Y. Tserkovnyak, and D. Loss, Phys. Rev. B **87**, 024402 (2013).

[11] S. Rohart, J. Miltat, and A. Thiaville, Phys. Rev. B **93**, 214412 (2016).

[12] A. Samoilenka and Y. Shnir, Phys. Rev. D **95**, 045002 (2017).

[13] R. A. Battye and M. Haberichter, Phys. Rev. D **88**, 125016 (2013).

[14] P. Jennings and T. Winyard, J. High Energy Phys. 01 (2014) 122.

[15] S. Tsesses, E. Ostrovsky, K. Cohen, B. Gjonaj, N. Lindner, and G. Bartal, Science **361**, 993 (2018).

[16] W. Legrand, D. Maccariello, F. Ajejas, S. Collin, A. Vecchiola, K. Bouzehouane, N. Reyren, V. Cros, and A. Fert, Nat. Mater. **19**, 34 (2020).

[17] C. Schütte and M. Garst, Phys. Rev. B **90**, 094423 (2014).

[18] V. P. Kravchuk, D. D. Sheka, U. K. Rößler, J. van den Brink, and Y. Gaididei, Phys. Rev. B **97**, 064403 (2018).

[19] S.-Z. Lin, C. D. Batista, and A. Saxena, Phys. Rev. B **89**, 024415 (2014).

[20] M. Kobayashi and M. Nitta, Phys. Rev. D **90**, 025010 (2014).

[21] S. Mühlbauer, B. Binz, F. Jonietz, C. Pfleiderer, A. Rosch, A. Neubauer, R. Georgii, and P. Böni, Science **323**, 915 (2009).

[22] G. Tatara and H. Fukuyama, J. Phys. Soc. Jpn. **83**, 104711 (2014).

[23] V. P. Kravchuk, D. D. Sheka, A. Kákay, O. M. Volkov, U. K. Rößler, J. van den Brink, D. Makarov, and Y. Gaididei, Phys. Rev. Lett. **120**, 067201 (2018).

[24] K.-y. Ho, T. R. Kirkpatrick, Y. Sang, and D. Belitz, Phys. Rev. B **82**, 134427 (2010).

[25] O. Petrova and O. Tchernyshyov, Phys. Rev. B **84**, 214433 (2011).

[26] Y.-H. Liu, Y.-Q. Li, and J. H. Han, Phys. Rev. B **87**, 100402(R) (2013).

[27] M. Nagao, Y.-G. So, H. Yoshida, K. Yamaura, T. Nagai, T. Hara, A. Yamazaki, and K. Kimoto, Phys. Rev. B **92**, 140415(R) (2015).

[28] M. Mruczkiewicz, P. Gruszecki, M. Zelent, and M. Krawczyk, Phys. Rev. B **93**, 174429 (2016).

[29] R. Zarzuela, S. K. Kim, and Y. Tserkovnyak, Phys. Rev. B **100**, 100408(R) (2019).

[30] M. Mochizuki, Phys. Rev. Lett. **108**, 017601 (2012).

[31] S.-Z. Lin and C. D. Batista, Phys. Rev. Lett. **120**, 077202 (2018).

[32] L. Rózsa, M. Weißenhofer, and U. Nowak, J. Phys.: Condens. Matter **33**, 054001 (2020).

[33] S. Seki, M. Garst, J. Waizner, R. Takagi, N. D. Khanh, Y. Okamura, K. Kondou, F. Kagawa, Y. Otani, and Y. Tokura, Nat. Commun. **11**, 256 (2020).

[34] X. Li, L. Shen, Y. Bai, J. Wang, X. Zhang, J. Xia, M. Ezawa, O. A. Tretiakov, X. Xu, M. Mruczkiewicz *et al.*, npj Comput. Mater. **6**, 169 (2020).

[35] X.-g. Wang, L. Chotorlishvili, G.-h. Guo, and J. Berakdar, J. Appl. Phys. **124**, 073903 (2018).

[36] U. Ritzmann, D. Hinzke, A. Kehlberger, E.-J. Guo, M. Kläui, and U. Nowak, Phys. Rev. B **92**, 174411 (2015).

[37] E.-J. Guo, J. Cramer, A. Kehlberger, C. A. Ferguson, D. A. MacLaren, G. Jakob, and M. Kläui, Phys. Rev. X **6**, 031012 (2016).

[38] V. E. Timofeev and D. N. Aristov, Phys. Rev. B **105**, 024422 (2022).

[39] Z. Wang, Y. Su, S.-Z. Lin, and C. D. Batista, Phys. Rev. B **103**, 104408 (2021).

[40] V. E. Timofeev, A. O. Sorokin, and D. N. Aristov, Phys. Rev. B **103**, 094402 (2021).

[41] H. Fukuyama and P. A. Lee, Phys. Rev. B **18**, 6245 (1978).

[42] C. A. Akosa, O. A. Tretiakov, G. Tatara, and A. Manchon, Phys. Rev. Lett. **121**, 097204 (2018).

[43] N. D. Mermin and H. Wagner, Phys. Rev. Lett. **17**, 1133 (1966).

[44] P. Bruno, Phys. Rev. Lett. **87**, 137203 (2001).

[45] P. Yan, A. Kamra, Y. Cao, and G. E. W. Bauer, Phys. Rev. B **88**, 144413 (2013).

[46] Y. Jiang, H. Y. Yuan, Z.-X. Li, Z. Wang, H. W. Zhang, Y. Cao, and P. Yan, Phys. Rev. Lett. **124**, 217204 (2020).

[47] C. Jia, D. Ma, A. F. Schäffer, and J. Berakdar, Nat. Commun. **10**, 2077 (2019).

[48] A. A. Thiele, Phys. Rev. Lett. **30**, 230 (1973).

[49] J. Seidel, *Topological Structures in Ferroic Materials. Domain Walls, Vortices and Skyrmions*, Springer Series in Materials Science (Springer International Publishing, Cham, Switzerland, 2016).

[50] W. Koshibae and N. Nagaosa, Sci. Rep. **7**, 42645 (2017).

[51] J. C. Martinez and M. B. A. Jalil, New J. Phys. **18**, 033008 (2016).